



Cite this: *Nanoscale*, 2016, 8, 233

# TiC<sub>2</sub>: a new two-dimensional sheet beyond MXenes†

Tianshan Zhao,<sup>a,b</sup> Shunhong Zhang,<sup>a,b</sup> Yaguang Guo<sup>a,b</sup> and Qian Wang<sup>\*a,b</sup>

MXenes are attracting attention due to their rich chemistry and intriguing properties. Here a new type of metal–carbon-based sheet composed of transition metal centers and C<sub>2</sub> dimers rather than individual C atom is designed. Taking the Ti system as a test case, density functional theory calculations combined with a thermodynamic analysis uncover the thermal and dynamic stability of the sheet, as well as a metallic band structure, anisotropic Young's modulus and Poisson's ratio, a high heat capacity, and a large Debye stiffness. Moreover, the TiC<sub>2</sub> sheet has an excellent Li storage capacity with a small migration barrier, a lower mass density compared with standard MXenes, and better chemical stability as compared to the MXene Ti<sub>2</sub>C sheet. When Ti is replaced with other transition metal centers, diverse new MC<sub>2</sub> sheets containing C≡C dimers can be formed, the properties of which merit further investigation.

Received 4th July 2015,  
Accepted 14th October 2015

DOI: 10.1039/c5nr04472c

[www.rsc.org/nanoscale](http://www.rsc.org/nanoscale)

## Introduction

Carbon, due to its unique flexibility to manipulate its four valence electrons in a very flexible way, forms diverse allotropes ranging from the well-known graphite and diamond to more recent C<sub>60</sub> fullerenes, nanotubes, nanochains, and to the newly discovered two-dimensional (2D) carbon like graphene,<sup>1</sup> graphyne,<sup>2</sup> graphdiyne,<sup>2</sup> and penta-graphene.<sup>3</sup> The unusual mechanical, electronic, optical, catalytic, and transport properties of these 2D carbon systems and their numerous technological applications have led to considerable interest in the study of other C-based 2D materials. One such example is the hotly pursued MXene type M<sub>n+1</sub>C<sub>n</sub> layers,<sup>4–7</sup> a group of 2D early transition metal (TM) carbides derived from chemical exfoliation of the MAX phases, where the concentration of the transition metal atoms (including Sc, Ti, V, Cr, Zr, Zb, Mo, Hf and Ta) exceeds that of carbon, and carbon is atomically bonded to the metal atoms. Because of their rich structural chemistry and good electronic conductivity, MXenes are promising candidates for applications in sensors, electronic devices, catalysts, conductive reinforcement additives to polymers, and electrochemical energy storage or conversion materials.<sup>8,9</sup> However, the main disadvantage of MXenes is that the metal atoms are highly exposed on the surfaces. In addition, the

surface functionalization is needed for applications in many cases.<sup>8,10</sup> Thus, it is necessary to go beyond the morphology of MXenes to design a new type of metal carbide sheet where the metal atoms are less than carbon and carbon is bonded molecularly rather than atomically with the metal atoms. Such kind of sheets can not only reduce their mass density and exposed metal sites with improved chemical stability, but also have different properties due to the change of the binding mode.

In fact, the C<sub>2</sub> dimer is the basic structural unit in the growth of many carbon structures such as fullerenes, nanotubes, graphene, and graphyne,<sup>2,11–14</sup> and even emerges on the reconstructed diamond surface.<sup>15</sup> C<sub>2</sub> is also the building unit of diverse carbon compounds such as metallocarbohedrenes (Met-Cars) M<sub>m</sub>C<sub>n</sub>,<sup>16,17</sup> metal-alkynide complexes,<sup>18</sup> alkynide complexes,<sup>19</sup> organic materials,<sup>20</sup> and some binary or ternary metal carbides (LiAgC<sub>2</sub>, KAgC<sub>2</sub>, CsAgC<sub>2</sub> and NaPdC<sub>2</sub>).<sup>21,22</sup> The first member of the Met-Cars family, Ti<sub>8</sub>C<sub>12</sub>, was discovered in 1992 by the Castleman group,<sup>16</sup> then the other members, M<sub>8</sub>C<sub>12</sub> with M = Sc, Zr, Hf, V, Nb, Ta, Cr, Mo, and Fe, were also synthesized<sup>23,24</sup> and joined in the family soon afterward. The common structural feature of these Met-Cars is that the six C<sub>2</sub> dimers are connected by eight TM atoms, forming cage-like structures. In addition, the C<sub>2</sub> molecule is a well-known pseudo-oxygen unit with an electron affinity (EA) of 3.4 eV which is nearly three times as large as that of a carbon atom. It has been demonstrated that the C<sub>2</sub> dimers play a key role in stability during the growth of Met-Cars where the clusters containing C<sub>2</sub> dimers are energetically more favorable than the structures containing only individual carbon atoms or trimers.<sup>25</sup> More interestingly, the C<sub>2</sub> dimers are also found to exist in both low and high carbon steels.<sup>26,27</sup>

<sup>a</sup>Center for Applied Physics and Technology, College of Engineering, Peking University, Beijing 100871, China

<sup>b</sup>IFSA Collaborative Innovation Center, and Key Laboratory of High Energy Density Physics Simulation, Ministry of Education, Beijing 100871, China.

E-mail: [qianwang2@pku.edu.cn](mailto:qianwang2@pku.edu.cn)

†Electronic supplementary information (ESI) available. See DOI: 10.1039/c5nr04472c

Despite the versatility of the  $C_2$  dimer in forming diverse structures, there has been no report to date on a 2D crystal that consists of transition metal atoms and  $C_2$  dimers. In MXenes<sup>4,8</sup> and other theoretically predicted metal carbide sheets,<sup>28</sup> the carbon atoms bind to the metal atoms individually. Here we present a comprehensive theoretical study of a 2D sheet composed of transition metal centers and  $C_2$  dimers by taking the Ti system as an example. The calculated results reveal that the  $TiC_2$  sheet is not only stable dynamically and thermally, but also it is metallic with outstanding Li storage capacity beyond existing MXene  $Ti_2C$  layers. Like MXene  $Ti_2C$ , the Ti in  $TiC_2$  could also be replaced with other transition metal elements, thus giving rise to a new type of 2D metal carbides  $MC_2$  with exceptional properties.

## Computational methods

Atomic structure optimizations and electronic structure calculations are carried out using density functional theory (DFT) as implemented in the Vienna *Ab initio* Simulation Package (VASP).<sup>27</sup> The projector augmented wave (PAW) method<sup>29</sup> and Perdew–Burke–Ernzerhof (PBE) exchange correlation functional within generalized gradient approximation (GGA)<sup>30</sup> are used. The  $2s^1$ ,  $2s^2 2p^2$  and  $3d^3 4s^1$  atomic orbitals are treated as valence states for Li, C, and Ti, respectively. Plane waves with a kinetic energy cutoff of 500 eV are used to expand the valence electron wave functions. For all structural relaxations the convergence criteria for total energy and Hellmann–Feynman force are set to be  $10^{-4}$  eV and  $10^{-2}$  eV  $\text{\AA}^{-1}$ , respectively. A unit cell with a vacuum space of 20  $\text{\AA}$  in a direction perpendicular to the nanosheet is used in order to avoid virtual interactions. The first Brillouin zone is sampled by a  $7 \times 7 \times 1$   $k$ -point grid within the Monkhorst–Pack scheme.<sup>31</sup> To check the dynamic stability, we use density functional perturbation theory (DFPT) to calculate the force constants. The Phonopy code<sup>32</sup> is used to calculate the vibrational spectra. *Ab initio* molecular dynamics (AIMD) simulations are also performed to assess the thermal stability of the  $TiC_2$  sheet. Canonical (NVT) ensemble is adopted using the Nosé heat bath method.<sup>33</sup> Bader charge analysis<sup>34</sup> is carried out to study the charge distribution and transfer quantitatively. By using the nudged elastic band (NEB) method,<sup>35</sup> we calculate the diffusion energy barrier and the minimum energy pathway of Li diffusion on the  $TiC_2$  sheet.

## Results and discussion

### Geometry and stability

The most well-known carbon–metal nanostructure containing  $C_2$  units is the  $Ti_8C_{12}$  Met-Car that was initially suggested to have  $T_h$  symmetry where 20 atoms form a nearly regular pentagonal dodecahedron,<sup>16,17</sup> as shown in Fig. 1a. However, the  $Ti_8C_{12}$  all-pentagon cage structure was later found to be unstable and transformed to a  $C_{3v}$ -like structure<sup>17</sup> (Fig. 1b). Rohmer *et al.*<sup>36</sup> analyzed all the possible structures of the

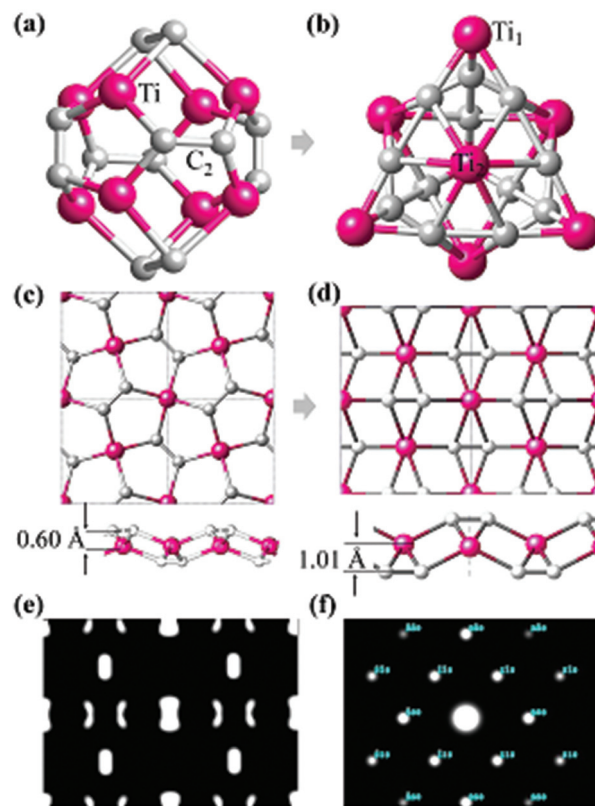


**Fig. 1** (a) Dodecahedral configuration of the  $Ti_8C_{12}$  cage with  $T_h$  symmetry. (b) Ground state configuration of the  $Ti_8C_{12}$  cage with  $C_{3v}$  symmetry.  $Ti_1$  and  $Ti_2$  refer to the Ti atoms with the EOC and SOC binding modes, respectively. (c) An all-pentagon  $TiC_2$  sheet derived from penta-graphene. (d) Optimized structure of the  $TiC_2$  sheet starting from the structure in (c). (e) and (f) Simulated STM and TEM images of the optimized  $TiC_2$  sheet, respectively.

$Ti_8C_{12}$  cluster, and found that the 8 Ti atoms forms a pseudocubic framework, each  $C_2$  unit could be oriented along one or other diagonal of the underlying face of the pseudocubic framework, independent of other dicarbon fragments. Following such an idea, we use a planar triangular Ti lattice like the first layer of (0001) surface of hcp bulk Ti, and build a 2D Ti–C sheet by depositing the  $C_2$  dimers on the surface with different positions and orientations, yielding three candidate structures with a chemical formula  $TiC_2$ , as shown in Fig. S1.† It is interesting to note that the most stable configuration (Fig. 1d) has the same geometry as optimized from penta-graphene like structure (Fig. 1c). Different from MXenes,<sup>4,9,10,37</sup> in the stable  $TiC_2$  sheet, Ti atoms are sandwiched between the top and bottom  $C_2$  layers, leading to a quasi-2D sheet with no exposed Ti atoms on the surfaces. Another difference between  $TiC_2$  and the MXene layers is that in MXenes, the carbon atoms are atomically bonded to its neighboring TM atoms with the C–C distance in the range of 2.80 to 3.35  $\text{\AA}$ ,<sup>4,9,11,38</sup> while the C–C distance in  $TiC_2$  is only 1.33  $\text{\AA}$ , showing a double bond character,<sup>39</sup> and implying that the carbon atoms exist in the form of a  $C_2$  dimer. In addition, unlike the MXenes that have hexa-

gonal symmetry,<sup>4</sup>  $\text{TiC}_2$  has a rectangular lattice with the optimized lattice parameters of  $a = 4.96 \text{ \AA}$  and  $b = 3.59 \text{ \AA}$ . The C–C bond in  $\text{TiC}_2$  is also stronger than that in the dodecahedral  $\text{Ti}_8\text{C}_{12}$  cage where the C–C bond length is  $1.40 \text{ \AA}$ ,<sup>16</sup> and is comparable to that in the  $\text{C}_{3v}$ -like structure ( $1.34 \text{ \AA}$ ).<sup>17</sup> Note that in bulk metal carbides the C–C bond can vary from conventional single bonds to typical triple bonds.<sup>39</sup>

To study the possible reasons why the structures in Fig. 1a and c are less stable than those in Fig. 1b and d, respectively, we have carefully checked their bonding features and found that in the  $T_h$  cage structure, all  $\text{C}_2$  dimers bind with the Ti atoms in an end-on configuration (EOC),<sup>40</sup> while in the  $\text{C}_{3v}$ -like structure<sup>41</sup> besides the EOC binding for some Ti atoms (labeled as  $\text{Ti}_1$  in Fig. 1b), the  $\text{C}_2$  dimers also bind with Ti in a side-on configuration (SOC) (labeled such Ti atoms as  $\text{Ti}_2$ ). Similarly, the pentagon based sheet (Fig. 1c) only contains the EOC binding mode, while the three-atomic-layer sheet (Fig. 1d) has both the EOC and SOC binding modes. The corresponding Ti–C bond length in the EOC and SOC modes is  $2.05 \text{ \AA}$  and  $2.20 \text{ \AA}$ , respectively, close to that of  $2.10 \text{ \AA}$  in the  $\text{Ti}_2\text{C}$  MXene monolayer.<sup>42</sup> In fact, it has been demonstrated experimentally and theoretically that the SOC binding mode is more energetically favorable over the EOC mode in the Met-Car structures.<sup>17,36,43–45</sup> Therefore, containing the SOC binding mode is the possible reason why the  $\text{C}_{3v}$ -like structure is more stable than the pentagonal dodecahedron as is also the case with the  $\text{TiC}_2$  sheet which adopted the configuration containing the SOC mode. The simulated Scanning Tunneling Microscopy (STM) (using the constant height model<sup>46</sup> with a height of  $0.9 \text{ \AA}$  and a negative bias of  $0.05 \text{ V}$ ) and Transmission Electron Microscopy (TEM)<sup>47,48</sup> (base on the so-called independent atom model which is also called the procrystal model<sup>49</sup>) images of the optimized  $\text{TiC}_2$  sheet are given in Fig. 1e and f for convenience in comparison with the experimental results in future.

The thermodynamic stability of the 2D  $\text{TiC}_2$  structure was studied by carrying out additional calculations with many

other possible structural isomers. For instance, two energetically low-lying isomers are given in Fig. S2a and S2b,<sup>†</sup> which are also composed of  $\text{C}_2$  units and Ti atoms with square and rectangular lattices, respectively. The former one contains both the EOC and SOC binding modes, while the latter has the EOC mode only. The optimized structures are given in Fig. S2c and S2d.<sup>†</sup> Total energy calculations show that these two structures are respectively  $0.75$  and  $0.78 \text{ eV}$  per formula unit (f. u.) higher in energy than the structure given in Fig. 1d. The underlying reason is that the binding mode is different in these three configurations. In Fig. S2d,<sup>†</sup> the binding between the Ti and  $\text{C}_2$  units is EOC only, while in Fig. S2c,<sup>†</sup> although the SOC binding mode also exists, the two neighboring  $\text{C}_2$  units are perpendicular to each other, which also differ from the parallel alignment of the  $\text{C}_2$  units in Fig. 1d. Thus, the resulting stresses make the two structures energetically unfavorable as compared to the one shown in Fig. 1d. We also compare the thermodynamic stability of the  $\text{TiC}_2$  sheet with some previously identified Ti–C compounds with other stoichiometry. Detailed discussion can be found in the ESI.<sup>†</sup>

We now focus on the energetically most stable structure of the  $\text{TiC}_2$  sheet. The phonon frequencies and phonon density of states (DOS) are calculated with high accuracy to examine its dynamical stability. The calculated results are summarized in Fig. 2, which show that the  $\text{TiC}_2$  sheet is dynamically stable as no imaginary frequencies exist in the entire Brillouin zone. The vibrational modes below  $350 \text{ cm}^{-1}$  including the three acoustic bands and three optical bands are mainly contributed by Ti due to its larger atomic mass.<sup>50</sup> The two highest optical modes are separated from others by a large phonon gap of around  $800 \text{ cm}^{-1}$ . Comparing the peaks of phonon PDOS with the phonon bands, the following features are identified: the  $z$  direction displacement pattern of the Ti atoms ( $\text{Ti}_z$ ) contributes to the  $z$  direction acoustic branch (ZA), the  $y$  direction displacement pattern ( $\text{Ti}_y$ ) constitutes the transverse acoustic branch (TA), and the longitudinal acoustic (LA) branch is formed by the displacement of Ti along the  $x$  direction ( $\text{Ti}_x$ ).

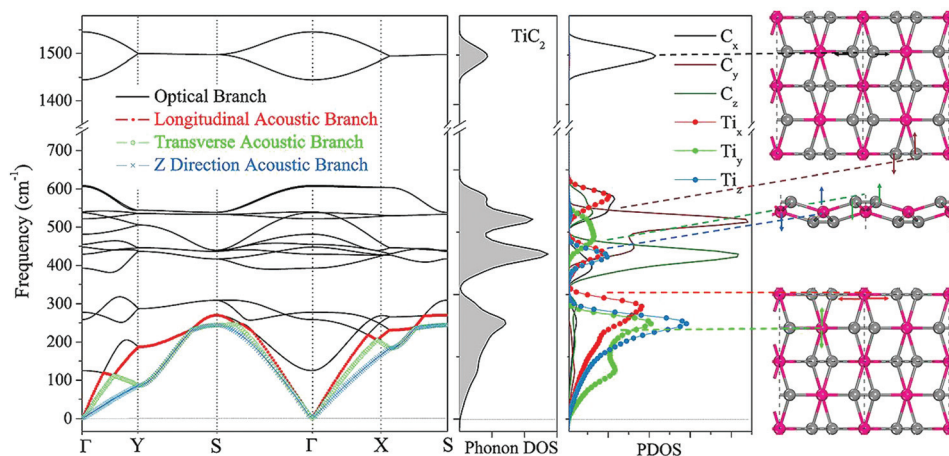


**Fig. 2** Phonon dispersion, and total and partial phonon DOS of the  $\text{TiC}_2$  sheet. Some characteristic vibrational modes are indicated in the rightmost column.

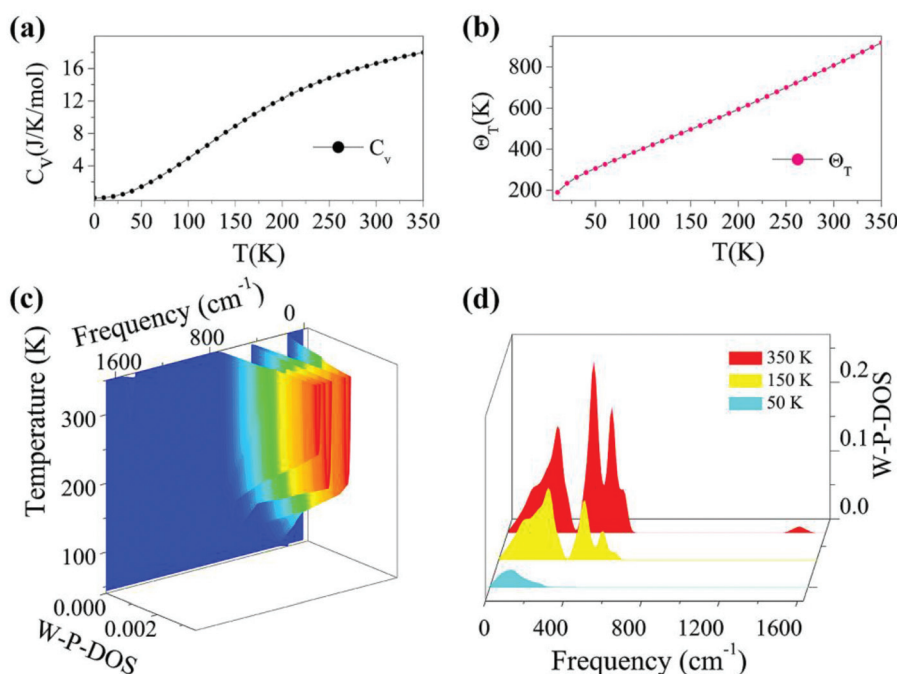


**Fig. 3** (a) Heat capacity, and (b) Debye temperature with respect to temperature of the  $\text{TiC}_2$  sheet; (c) 3D plot of the weighted phonon DOS (W-P-DOS) as a function of frequency and temperature; (d) cross sections of the W-P-DOS at 50, 150 and 350 K.

The  $C_y$  and  $C_z$  vibrations make main contributions to the optical bands between  $350\text{ cm}^{-1}$  and  $650\text{ cm}^{-1}$ . The stretching mode of the  $\text{C}=\text{C}$  bonds ( $C_x$ ) corresponds to the two highest optical branches. The highest optical mode reaches up to  $1600\text{ cm}^{-1}$ , which is comparable to that of the  $\text{C}=\text{C}$  bonds in recently reported carbon structures,<sup>3,51</sup> but it is higher than that of the  $\text{Ti}_8\text{C}_{12}$  cluster ( $1360\text{ cm}^{-1}$ )<sup>52</sup> due to the different bond orders.

To study the thermal stability of the  $\text{TiC}_2$  sheet at finite temperature, we perform AIMD simulations at 350 K using a relatively large ( $4 \times 4$ ) supercell as a small unit cell may easily result in false instability. The time step is set as 1 femtosecond (fs). After 5 picoseconds of simulation, no structural distortion or reconstruction is found, and the average total potential energy remains nearly constant as shown in Fig. S5,<sup>†</sup> confirming that  $\text{TiC}_2$  is thermally stable at room temperature. The thermal stability of  $\text{TiC}_2$  provides the possibility of its future synthesis and application under ambient conditions.

### Thermodynamic properties

Based on the calculated phonon spectrum, a series of thermodynamic properties can be derived. Here we concentrate on studies of the heat capacity and Debye temperature of the  $\text{TiC}_2$  sheet. The calculated phonon heat capacity with respect to temperature is plotted in Fig. 3a. The heat capacity can also be expressed using the phonon DOS.<sup>53</sup> The Debye temperature  $\Theta_D = \hbar\nu_D/k_B$  is determined by fitting the calculated  $C_V$ - $T$  curve using the Debye model. The fitted Debye temperature  $\Theta_D(T)$  is given in Fig. 3b, which shows that the  $\Theta_D(T)$  is as high as

850 K at room temperature. Since the vibrational frequency is proportional to the square root of the stiffness within the harmonic approximation,  $\Theta_D$  can be used as a measurement of the “stiffness” of solids.<sup>53</sup> Therefore, from Fig. 3b we see that the  $\text{TiC}_2$  sheet can display large Debye stiffness due to its high Debye temperature, resulting from covalent  $\text{C}=\text{C}$  bonds.

As the phonons are subjected to Bose-Einstein distribution, the weighted phonon DOS  $g(\nu)W(\hbar\nu/k_B T)$  describes the contribution of vibrational modes with a certain frequency to the heat capacity. The frequency and temperature dependence of the weighted phonon DOS is plotted in Fig. 3c. We find that at 50 K, only about 2.5% or even less weighting factor  $W(\hbar\nu/k_B T)$  exists in the frequency region over  $400\text{ cm}^{-1}$ , indicating that only low-frequency states contribute to the heat capacity at low temperature. This is evidenced by Fig. 3d showing the variation of the weighted phonon DOS with respect to frequency at different temperatures. Since the heat capacity defined by the Debye model is proportional to the cross section of frequency-phonon DOS at a given temperature, a larger amount of heat is required to increase the temperature by one Kelvin when the cross section is larger. Because  $\text{TiC}_2$  has more vibrational states than graphite and diamond<sup>53</sup> in the low frequency region,  $\text{TiC}_2$  exhibits larger heat capacity under 350 K.

### Mechanical properties

To further investigate how lattice distortions affect the structural stability of  $\text{TiC}_2$ , we first calculate the elastic constants to examine its mechanical stability. The elastic constants are calculated to be:  $C_{11} = 140.58\text{ N m}^{-1}$ ,  $C_{22} = 70.52\text{ N m}^{-1}$ ,  $C_{12} =$



$25.10 \text{ N m}^{-1}$ , and  $C_{44} = 16.19 \text{ N m}^{-1}$ . Obviously, they satisfy the Born criteria,<sup>54,55</sup> namely,  $C_{11}, C_{22}, C_{44} > 0$  and  $C_{11}C_{22} - C_{12}^2 > 0$ , suggesting that the  $\text{TiC}_2$  sheet is mechanically stable. Based on the obtained elastic constants,<sup>56</sup> the Young's modulus  $E(\theta)$  and Poisson's ratio  $\nu(\theta)$  along an arbitrary in-plane direction  $\theta$  ( $\theta$  is the angle relative to the  $x$  direction) are calculated using the formula:<sup>57</sup>

$$E(\theta) = \frac{C_{11}C_{22} - C_{12}^2}{C_{11}s^4 + C_{22}c^4 + \left(\frac{C_{11}C_{22} - C_{12}^2}{C_{44}} - 2C_{12}\right)c^2s^2} \quad (1)$$

$$\nu(\theta) = -\frac{\left(C_{11} + C_{22} - \frac{C_{11}C_{22} - C_{12}^2}{C_{44}}\right)c^2s^2 - C_{12}(s^4 + c^4)}{C_{11}s^4 + C_{22}c^4 + \left(\frac{C_{11}C_{22} - C_{12}^2}{C_{44}} - 2C_{12}\right)c^2s^2} \quad (2)$$

where  $c = \cos \theta$  and  $s = \sin \theta$ . The results are plotted in Fig. 4. The deviations of  $E(\theta)$  and  $\nu(\theta)$  from the perfect circles indicate the elastic anisotropy of the  $\text{TiC}_2$  sheet, which results from the fact that all the  $\text{C}=\text{C}$  units are aligned parallel in the  $x$  direction. The Young's modulus in the  $x$  and  $y$  directions are found to be  $E_x = 131.17 \text{ N m}^{-1}$  and  $E_y = 66.04 \text{ N m}^{-1}$ , respectively.  $E_x$  is close to that of MXene  $\text{Ti}_2\text{C}$  ( $130 \text{ N m}^{-1}$ ).<sup>42</sup> In the  $y$  direction, the Ti atoms bind to the  $\text{C}_2$  units through the interaction between Ti-3d and  $\pi$  orbitals of the C-C dimer. Because this interaction is weaker than the  $\text{C}=\text{C}$  bond, it results in a small value of  $E_y$ , being only half of  $E_x$ . Poisson's ratio is also a fundamental parameter describing the mechanical behavior of a material. For a perfectly incompressible and isotropic material, the Poisson's ratio is exactly equal to 0.5.<sup>58</sup> However, Fig. 4b shows that for the anisotropic  $\text{TiC}_2$  sheet, the Poisson's ratio reaches 0.59 in some directions, which is much larger than that of MXene  $\text{Ti}_2\text{C}$  (0.23). For comparison, the main results of the elastic constants, Young's modulus, and Poisson's ratio of  $\text{TiC}_2$  and other 2D layers are listed in Table 1.<sup>56,58–60</sup>

### Electronic properties

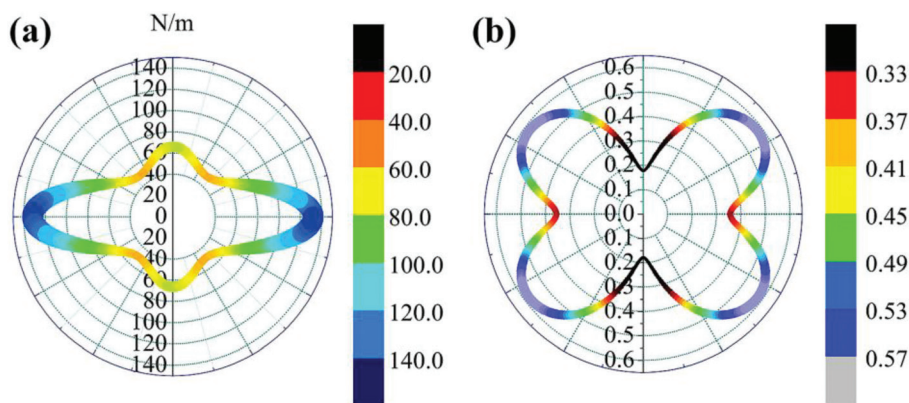
To study the electronic properties we calculate the electronic band structure of the  $\text{TiC}_2$  sheet. The results are plotted in

**Table 1** Elastic constants of  $C_{11}$  and  $C_{12}$ , in-plane Young's modulus  $Y$ , and Poisson's ratio  $\nu$  of the 2D  $\text{TiC}_2$ ,  $\text{Ti}_2\text{C}$ , graphene,  $\text{MoS}_2$ , and h-BN sheets

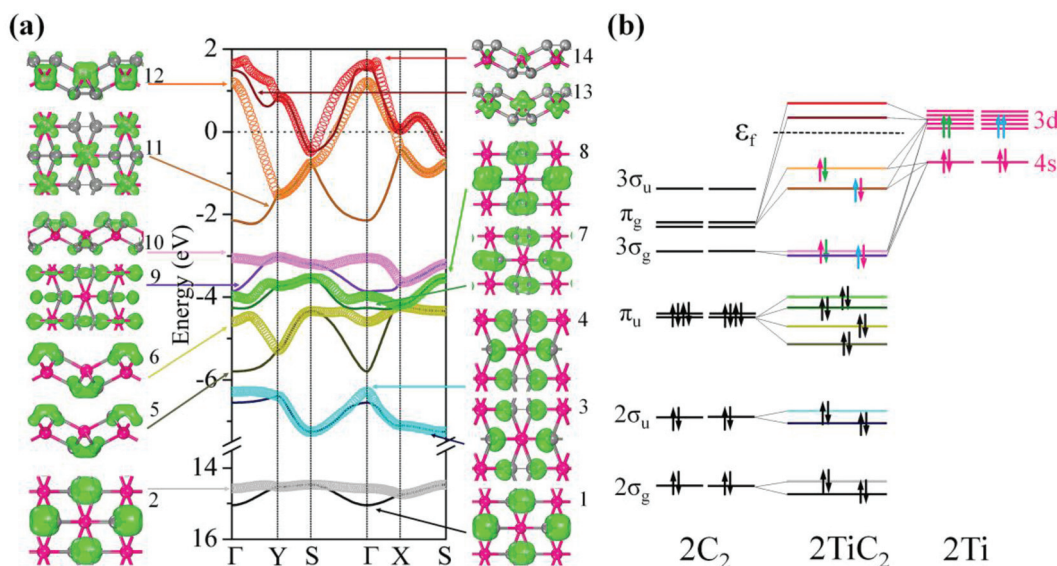
Materials	Elastic constants ( $\text{N m}^{-1}$ )		$Y$ ( $\text{N m}^{-1}$ )	$\nu$
	$C_{11}$	$C_{22}$		
$\text{TiC}_2$	141	71	131(x) 61(y)	0.59(max) 0.21(min)
$\text{Ti}_2\text{C}^{42}$	137	32	130	0.23
Graphene <sup>59</sup>	353	61	342	0.17
$\text{MoS}_2^{60}$	140	40	129	0.31
h-BN <sup>56</sup>	335	89	318	0.27

Fig. 5a.  $\text{TiC}_2$  is found to be metallic as the partially occupied bands, namely the bands numbered as 12, 13, and 14, cross the Fermi level in the Brillouin zone. The metallicity is further confirmed by using the more accurate HSE06 functional.<sup>61,62</sup> Orbital analysis suggests that the bands near the Fermi level are dominated by the Ti-3d orbitals, while the C-2s and 2p orbitals also make small contributions to the observed metallicity through hybridization with the Ti-3d states. We further calculate the band-decomposed charge densities and plot them in Fig. 5a as well. By carefully examining the charge distribution of each band, we clarify the interactions between the frontier orbitals of the  $\text{C}_2$  units and the Ti atoms, as illustrated in Fig. 5b. The ground state electronic configuration of an isolated  $\text{C}_2$  dimer is  $(1\sigma_g)^2(1\sigma_u)^2(2\sigma_g)^2(2\sigma_u)^2(1\pi_u)^4$  with the higher states  $(3\sigma_g)(1\pi_g)(3\sigma_u)$  unoccupied. The Ti atoms form a slightly distorted triangular sublattice, akin to that in the recently predicted  $\text{TiB}_2$ .<sup>63</sup> The Ti-3d orbitals split into  $e_1(d_{xy}, d_{xx-yy})$ ,  $e_1'(d_{xz}, d_{yz})$ , and  $a^*(d_{zz})$  in a triangular crystal field. For comparison, we plot the energy bands formed by the sublattices of the  $\text{C}_2$  units and the Ti atoms in Fig. S6,<sup>†</sup> respectively.

In Fig. 5a, 1<sup>st</sup> to 8<sup>th</sup> energy bands with energy ranging from  $-15$  to  $-3.5 \text{ eV}$  correspond to the  $2\sigma_g$  (bonding),  $2\sigma_u$  (anti-bonding), and  $\pi_u$  (bonding) states of the  $\text{C}_2$  units, and lie deep under the Fermi level because their energies are much lower



**Fig. 4** Polar diagrams of (a) Young's modulus  $E(\theta)$  and (b) Poisson's ratio  $\nu(\theta)$  of the  $\text{TiC}_2$  sheet.



**Fig. 5** (a) Electronic band structure, and decomposed charge density distributions (isovalued:  $0.1 \text{ e } \text{\AA}^{-3}$ ) for each band with the corresponding band index denoted of the  $\text{TiC}_2$  sheet near the Fermi level. The Fermi energy is set to 0 eV. The high symmetry  $k$  point path is along:  $\Gamma(0, 0) \rightarrow Y(0, 1/2) \rightarrow S(1/2, 1/2) \rightarrow \Gamma(0, 0) \rightarrow X(1/2, 0) \rightarrow S(1/2, 1/2)$ . (b) Schematic diagram showing the interactions between the frontier orbitals of the  $\text{C}_2$  units and the Ti atoms (note that there are two  $\text{C}_2$  units and two Ti atoms in a unit cell of  $\text{TiC}_2$ ).

than that of the Ti-3d states. The  $\text{C}_2$ - $3\sigma_g$  and  $\pi_g$  states hybridize with the Ti-3d and 4s states, forming the three fully occupied bands (the 9<sup>th</sup>, 10<sup>th</sup>, and 11<sup>th</sup> bands) and three partially occupied bands (the 12<sup>th</sup>, 13<sup>th</sup>, and 14<sup>th</sup> bands). The bands with energy higher than 2.0 eV are unoccupied and hence are not given in the band structure. To visualize the charge distribution, we plot the band-decomposed charge density iso-surfaces for each individual band of the band structure in Fig. 5a, which clearly show the main contribution to the charge density of each band. For instance, the band-decomposed charge densities of the 9<sup>th</sup> and 10<sup>th</sup> bands mainly aggregate in the proximity of  $\text{C}_2$ , indicating that the  $\text{C}_2$ - $3\sigma_g$  orbitals are filled by the electrons of Ti donors in this 2D crystal. This is qualitatively consistent with our Bader charge analysis, which indicates that each Ti atom transfers about 1.5 electrons to each  $\text{C}_2$  unit. The bands near the Fermi level are dominated by the Ti-3d states, and consequently the corresponding band-decomposed charge accumulates around the Ti atoms. The band-decomposed charge densities of the 11<sup>th</sup> and 12<sup>th</sup> bands clearly show the characteristics of Ti- $3d_{xy}$  and  $3d_{xz}$  orbitals, respectively, while both the 13<sup>th</sup> and 14<sup>th</sup> bands have the feature of Ti- $3d_{zz}$  orbitals, indicating that the metallicity of  $\text{TiC}_2$  originates from the electrons in Ti- $3d_{xz}$  and  $3d_{zz}$  orbitals. Interestingly, we note that the orbital interactions in  $\text{TiC}_2$  are similar to those in bulk  $\text{UC}_2$ .<sup>39</sup> However, Ti-3d and 4s orbitals have much lower energy as compared to U-6d, which enables them to have a stronger interaction with the frontier orbitals of  $\text{C}_2$  units, leading to the stable 2D sheet.

We further discuss the influence of the occupation of  $\text{C}_2$  orbitals on the C=C bond length. It has been demonstrated that in  $\text{C}_2$  containing metal carbide systems, the more the

$\text{C}_2$ - $\pi_u$  bonding orbital is occupied, or the less the  $\text{C}_2$ - $\pi_g$  anti-bonding orbital is filled, the shorter is the C=C bond length.<sup>39</sup> The ground state of the isolated  $\text{C}_2$  has an equilibrium C-C distance of 1.31 Å. The reason that the C-C bond length (1.33 Å) in  $\text{TiC}_2$  is slightly longer than that of an isolated  $\text{C}_2$  dimer is because the  $\text{C}_2$ - $\pi_g$  orbital is partially occupied.

### Potential applications of $\text{TiC}_2$ as an anode material in lithium ion battery

The metallicity of  $\text{TiC}_2$  provides an intrinsic advantage in electrical conductivity as compared to semiconducting or insulating transition-metal oxides and TMD layers. Therefore, it may find applications as electrodes. In fact, recently MXenes have been widely studied both theoretically and experimentally as promising anode materials for Li ion batteries (LIBs).<sup>64,65</sup> Considering that  $\text{TiC}_2$  possesses higher carbon content as compared to the MXene  $\text{Ti}_2\text{C}$ , we expect that this sheet can have a better Li storage capacity. In the following, we systematically explore the possibility of  $\text{TiC}_2$  as a LIB anode material by looking at the adsorption and diffusion behaviors of Li atoms on this sheet, and derive the relative electrochemical properties of the Li adsorbed  $\text{TiC}_2$ .

To determine the preferable adsorption site of Li on the  $\text{TiC}_2$  sheet, we use a  $2 \times 2$  supercell and deposit one Li atom on different sites, corresponding to a stoichiometry of  $\text{Ti}_8\text{C}_{16}\text{Li}$ . Four typical adsorption configurations with high structural symmetry, labeled as  $C_I$ ,  $C_{II}$ ,  $C_{III}$  and  $C_{IV}$ , are considered, as shown in Fig. 6a, where  $C_I$  is the hollow site of the four neighboring carbon dimers,  $C_{II}$  is the on-top site of Ti that is in between the two neighboring C=C units lying along

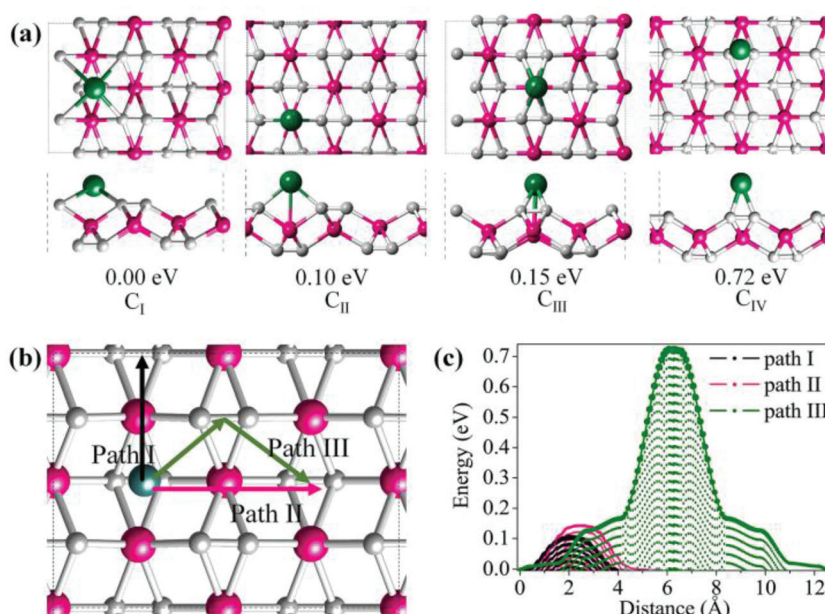


Fig. 6 (a) Four optimized configurations of the Li-adsorbed TiC<sub>2</sub> sheet (Ti<sub>8</sub>C<sub>16</sub>Li) and their relative energies with respect to the lowest energy configuration C<sub>I</sub>. (b) Considered migration paths of Li diffusion on the TiC<sub>2</sub> sheet, and (c) the corresponding diffusion energy barrier profiles.

a line, C<sub>III</sub> is the on-top site of Ti that is in between the two parallel C=C units lying in two neighboring lines, and C<sub>IV</sub> is the bridge site of the C=C units. Full geometry optimizations and total energy calculations are performed to identify their relative stability. C<sub>I</sub> is found to be the lowest energy configuration with energy by 0.10, 0.15 and 0.72 eV respectively lower than that of C<sub>II</sub>, C<sub>III</sub> and C<sub>IV</sub>, suggesting that the Li atom prefers to occupy the hollow site of the carbon dimers on the TiC<sub>2</sub> sheet.

To evaluate the potential application of the TiC<sub>2</sub> sheet as an anode material for LIB, we investigate the possible diffusion paths of the Li atom on this sheet and their corresponding energy barriers. We consider three trial diffusion paths that connect the two neighboring most preferable Li adsorption sites with high structural symmetry, as indicated in Fig. 6b. Pathway I is found to have the lowest diffusion barrier of 0.11 eV and the shortest diffusion length of 4.38 Å. The magnitude of energy barrier is even smaller than half of those of titanium carbide MXenes (see Table 2)<sup>10,64</sup> implying a good conductivity of the Li ions on the TiC<sub>2</sub> sheet, which is an important parameter for a LIB electrode material. When Li ions diffuse along path II (perpendicular to path I), the energy barrier is 0.16 eV. This is only 0.05 eV higher than that of path I. While the energy barrier is 0.76 eV when Li ions diffuse along path III, which is much larger than that of path I or path II. The variation of energy barrier with respect to the migration distance of Li on this sheet is plotted in Fig. 6c. Thus, it is clear that both path I and II are the possible routes for Li ion diffusion, which is beneficial for an electrode material.

After investigating the adsorption site and the migration path, we studied the adsorption of Li with high concentration.

Table 2 Comparison of specific capacity and diffusion barrier of candidate anode materials for the Li ion battery. "—" means data unavailable

Materials	Specific capacity (mA h g <sup>-1</sup> )		Diffusion barrier (eV)		OCV (V)
	Theo.	Expt.	Theo.	Expt.	
TiC <sub>2</sub>	622	—	0.11	—	0.96
Ti <sub>2</sub> C	440 <sup>10</sup>	—	0.27	—	0.44
Nb <sub>2</sub> C	253 <sup>10</sup>	—	—	—	0.52
V <sub>2</sub> C	419 <sup>10</sup>	—	—	—	0.47
Ti <sub>3</sub> C <sub>2</sub>	320 <sup>66</sup>	—	0.07	—	0.62
f-Ti <sub>3</sub> C <sub>2</sub>	449 <sup>64</sup>	410	0.28	—	—
Graphite	372	372	0.4 <sup>67</sup>	—	0.2
TiO <sub>2</sub>	200 <sup>68,69</sup>	200	—	0.35–0.65 <sup>70</sup>	1.8

It has been demonstrated that the weight percentage of Li can reach 9% on the surfaces of the functionalized MXenes and multi-layer Li adsorption has been achieved, which significantly enhances the Li storage capacity.<sup>64,65</sup> For the TiC<sub>2</sub> sheet, we first increase the concentration of Li from the stoichiometry of Ti<sub>8</sub>C<sub>16</sub>Li to Ti<sub>2</sub>C<sub>4</sub>Li. The preferable adsorption site of Li is again determined to be the hollow site by following the same procedure mentioned above. Based on Bader charge analysis, we find that each adsorbed Li atom transfers 0.86 electrons to the TiC<sub>2</sub> sheet. We then calculate the phonon spectrum to examine the effect of Li adsorption on the dynamic stability of the TiC<sub>2</sub> sheet at such a relatively high Li adsorption concentration. The calculated results are plotted in Fig. 7a, which shows that all the vibrational modes are real in the Brillouin zone, indicating that the adsorption of the Li atom does not



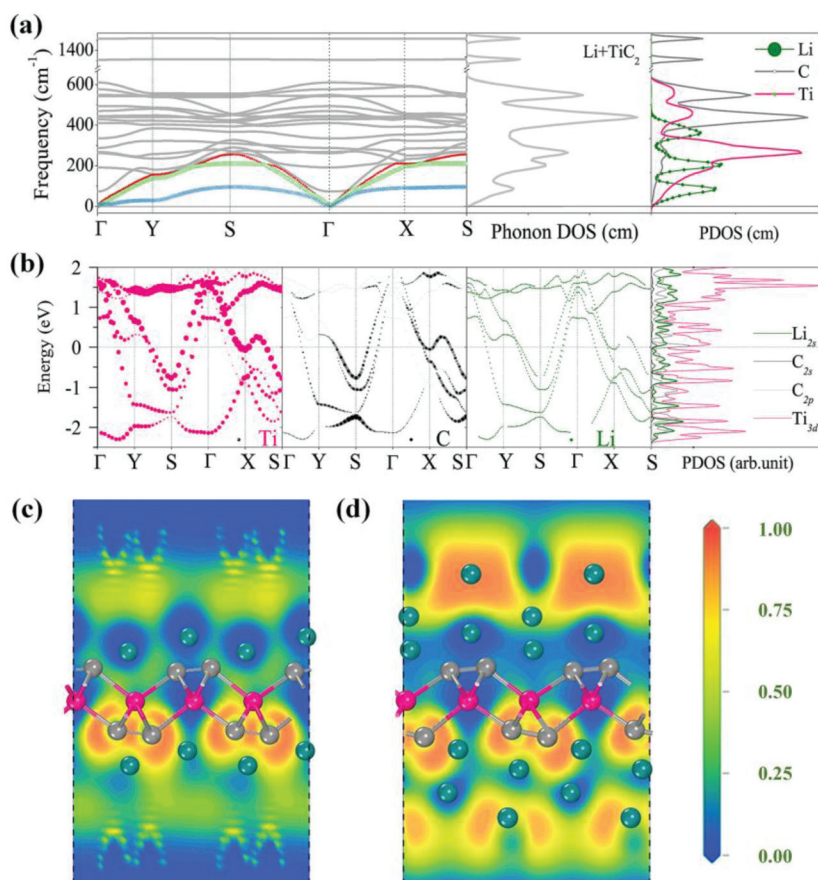


Fig. 7 (a) Phonon dispersion, phonon total and partial DOS, and (b) electronic band structure of  $\text{Ti}_2\text{C}_4\text{Li}$ . Band compositions are indicated with the size of circles. (c) and (d) ELF slices of the lithiated  $\text{TiC}_2$  sheet with stoichiometry of  $\text{TiC}_2\text{Li}_2$  and  $\text{TiC}_2\text{Li}_4$ , respectively.

disturb the dynamic stability of the  $\text{TiC}_2$  sheet. The total and partial phonon DOS are then plotted in Fig. 7a as well, showing that the vibrations of the adsorbed Li atoms mainly contribute to the acoustic modes at the low frequency region.

To study the effect of high Li concentration on the electronic structure, we calculated the electronic band structure of the  $\text{Ti}_2\text{C}_4\text{Li}$  sheet and compared it with that of the pristine  $\text{TiC}_2$  sheet. We noted that the number of energy bands crossing the Fermi level increases upon Li adsorption, as shown in Fig. 7b, and the interaction between Li and Ti orbitals in the vicinity of the Fermi level is weak due to the repulsive interactions between the Ti and Li ions.

We further increased the concentration of Li by depositing a single layer of Li atoms on both the sides of the  $\text{TiC}_2$  sheet, leading to a stoichiometry of  $\text{TiC}_2\text{Li}_2$  (corresponding to a weight percentage of Li of 16.2%). The electrons over the Li layer form negatively charged cloud, the same is the case with MXenes.<sup>65</sup> This is visualized by the calculated electron localization functions (ELF) (Fig. 7c). The average adsorption energy for each Li ion in this situation is 0.96 eV. We then introduce one more layer of Li atoms on both sides of the lithiated  $\text{TiC}_2$  sheet, corresponding to a chemical ratio of  $\text{TiC}_2\text{Li}_4$ . The interaction between the two Li layers is visible from the calculated

ELF shown in Fig. 7d, indicating that the second Li layer is able to bind with the lithiated  $\text{TiC}_2$  sheet, as the negatively charged environment is favorable to the adsorption of the second Li layer. Here we see that the  $\text{TiC}_2$  sheet has a high Li storage capacity, this is very different from the MXene  $\text{Ti}_2\text{C}$  sheet which needs surface functionalization for ion intercalation batteries.<sup>65</sup>

In the following, we calculate the average open circuit voltage (OCV) and the theoretical Li storage capacity, which are important electrochemical properties of an electrode material. OCV can be directly derived in a rather simple way:<sup>66</sup>

$$\text{OCV} \approx [E(\text{TiC}_2) + xE(\text{Li}) - E(\text{TiC}_2\text{Li}_x)]/x \quad (3)$$

here  $E(\text{TiC}_2)$ ,  $E(\text{Li})$ , and  $E(\text{TiC}_2\text{Li}_x)$  represent the free energies (total energy at 0 K) of pristine  $\text{TiC}_2$ , Li in bcc bulk, and the Li-adsorbed  $\text{TiC}_2$ , respectively. For the one layer adsorption, the  $2 \times 2$  supercell can accommodate up to 16 Li atoms, corresponding to a stoichiometry of  $\text{TiC}_2\text{Li}_2$ . The estimated OCV is 0.96 V, and the theoretical capacity is calculated to be  $622 \text{ mA h g}^{-1}$ . When the two-layer adsorption is considered, the stoichiometry is  $\text{TiC}_2\text{Li}_4$ . At such high Li concentration, the OCV and theoretical specific capacity are 0.29 V and  $1226 \text{ mA h g}^{-1}$ , respectively, showing that the new type  $\text{TiC}_2$  sheet has much



higher Li storage capacity as compared to the previously reported  $M_{n+1}C_n$  type of MXenes. For instance, the theoretical specific capacity of  $Ti_2C$ ,<sup>10</sup>  $Ti_3C_2$ ,<sup>66</sup>  $Nb_2C$ ,<sup>10</sup> and  $V_2C$ <sup>10</sup> are 440 mA h g<sup>-1</sup>, 320 mA h g<sup>-1</sup>, 253 mA h g<sup>-1</sup>, and 419 mA h g<sup>-1</sup>, respectively. A comparison of our calculated specific capacity and diffusion barrier with several candidate anode materials for LIBs are given in Table 2.<sup>67–70</sup> The high Li storage capacity of  $TiC_2$  can be understood from the following facts: (i) when Li is adsorbed on the  $TiC_2$  sheet, it transfers more electrons to the sheet (0.86 e) as compared to that of Li on MXenes,<sup>66</sup> resulting in a smaller radius of Li cation and a weaker Coulomb repulsion. (ii) The  $TiC_2$  sheet has higher carbon content than MXenes, thus having a higher specific capacity. (iii)  $TiC_2$  has a lower mass areal density of 1.348 kg m<sup>-2</sup>, which is much smaller than that of the MXene  $Ti_2C$  sheet (2.246 kg m<sup>-2</sup>).<sup>42</sup>

## Conclusions

In conclusion, stimulated by the special role of the  $C_2$  dimer in the synthesis of many carbon-based materials as well as its special properties compared to the individual C atoms, we have explored a new type of 2D transition metal carbide by taking the  $TiC_2$  sheet as an example, which is composed of Ti centers and C=C dimers. Using the state-of-the-art theoretical calculations, we demonstrated that this sheet is not only dynamically, mechanically and thermally stable, but also exhibits exceptional properties including a metallic band structure, anisotropic elasticity, a large heat capacity and Debye stiffness. Due to its unique atomic configuration, the pristine  $TiC_2$  sheet has an outstanding Li storage capacity with a smaller migration energy barrier as compared with regular MXenes. In addition, compared to MXene  $Ti_2C$  sheets,  $TiC_2$  has less exposed metal sites on the surfaces showing better chemical stability and lower mass density (only 60% of the  $Ti_2C$  sheet). In short, as a new member of the 2D metal carbide family, the studied  $TiC_2$  sheet is unique as it contains C=C dimers instead of individual C atoms, and displays novel properties beyond MXenes.

## Acknowledgements

This work is partially supported by grants from the National Natural Science Foundation of China (NSFC-11174014 and NSFC-51471004), the National Grand Fundamental Research 973 Program of China (Grant No. 2012CB921404), and the Doctoral Program of Higher Education of China (20130001110033). The calculations were carried out in Shanghai supercomputer center.

## References

- 1 K. S. Novoselov, A. K. Geim, S. V. Morozov, D. Jiang, Y. Zhang, S. V. Dubonos, I. V. Grigorieva and A. A. Firsov, *Science*, 2004, **306**, 666–669.
- 2 Y. Li, L. Xu, H. Liu and Y. Li, *Chem. Soc. Rev.*, 2014, **43**, 2576–2582.
- 3 S. Zhang, J. Zhou, Q. Wang, X. Chen, Y. Kawazoe and P. Jena, *Proc. Natl. Acad. Sci. U. S. A.*, 2015, **112**, 2372–2377.
- 4 M. Naguib, M. Kurtoglu, V. Presser, J. Lu, J. Niu, M. Heon, L. Hultman, Y. Gogotsi and M. W. Barsoum, *Adv. Mater.*, 2011, **23**, 4248–4253.
- 5 M. Naguib and Y. Gogotsi, *Acc. Chem. Res.*, 2015, **48**, 128–135.
- 6 J.-C. Lei, X. Zhang and Z. Zhou, *Front. Phys.*, 2015, **10**, 276–286.
- 7 M. Kurtoglu, M. Naguib, Y. Gogotsi and M. W. Barsoum, *MRS Commun.*, 2012, **2**, 133–137.
- 8 M. Khazaei, M. Arai, T. Sasaki, C.-Y. Chung, N. S. Venkataramanan, M. Estili, Y. Sakka and Y. Kawazoe, *Adv. Funct. Mater.*, 2013, **23**, 2185–2192.
- 9 M. Naguib, V. N. Mochalin, M. W. Barsoum and Y. Gogotsi, *Adv. Mater.*, 2014, **26**, 992–1005.
- 10 C. Eames and M. S. Islam, *J. Am. Chem. Soc.*, 2014, **136**, 16270–16276.
- 11 F. Calvo, S. Diaz-Tendero and M. A. Lebeault, *Phys. Chem. Chem. Phys.*, 2009, **11**, 6345–6352.
- 12 Q. Wang, M.-F. Ng, S.-W. Yang, Y. Yang and Y. Chen, *ACS Nano*, 2010, **4**, 939–946.
- 13 M. Sternberg, P. Zapol and L. A. Curtiss, *Phys. Rev. B: Condens. Matter*, 2003, **68**, 205330.
- 14 L. Xu, Y. Jin, Z. Wu, Q. Yuan, Z. Jiang, Y. Ma and W. Huang, *J. Phys. Chem. C*, 2013, **117**, 2952–2958.
- 15 K. Bobrov, A. J. Mayne and G. Dujardin, *Nature*, 2001, **413**, 616–619.
- 16 B. C. Guo, K. P. Kerns and A. W. Castleman, *Science*, 1992, **255**, 1411–1413.
- 17 M.-M. Rohmer, M. Bénard and J.-M. Poblet, *Chem. Rev.*, 2000, **100**, 495–542.
- 18 N. J. Long and C. K. Williams, *Angew. Chem., Int. Ed.*, 2003, **42**, 2586–2617.
- 19 V. W.-W. Yam, *Acc. Chem. Res.*, 2002, **35**, 555–563.
- 20 T. P. Vaid, *J. Am. Chem. Soc.*, 2011, **133**, 15838–15841.
- 21 R. Buschbeck, P. J. Low and H. Lang, *Coord. Chem. Rev.*, 2011, **255**, 241–272.
- 22 A. L. Ivanovskii, A. A. Sofronov and Y. N. Makurin, *Theor. Exp. Chem.*, 1999, **35**, 270–274.
- 23 B. C. Guo, S. Wei, J. Purnell, S. Buzza and A. W. Castleman, *Science*, 1992, **256**, 515–516.
- 24 S. Wei, B. C. Guo, J. Purnell, S. Buzza and A. W. Castleman, *Science*, 1992, **256**, 818–820.
- 25 J.-O. Joswig and M. Springborg, *J. Chem. Phys.*, 2008, **129**, 134311.
- 26 A. T. Paxton and C. Elsässer, *Phys. Rev. B: Condens. Matter*, 2013, **87**, 224110.
- 27 G. Kresse and J. Furthmüller, *Phys. Rev. B: Condens. Matter*, 1996, **54**, 11169–11186.
- 28 Z. Zhang, X. Liu, B. I. Yakobson and W. Guo, *J. Am. Chem. Soc.*, 2012, **134**, 19326–19329.
- 29 P. E. Blöchl, *Phys. Rev. B: Condens. Matter*, 1994, **50**, 17953–17979.

- 30 J. P. Perdew, K. Burke and M. Ernzerhof, *Phys. Rev. Lett.*, 1996, **77**, 3865–3868.
- 31 H. J. Monkhorst and J. D. Pack, *Phys. Rev. B: Solid State*, 1976, **13**, 5188–5192.
- 32 A. Togo, F. Oba and I. Tanaka, *Phys. Rev. B: Condens. Matter*, 2008, **78**, 134106.
- 33 S. Nosé, *J. Chem. Phys.*, 1984, **81**, 511–519.
- 34 W. Tang, E. Sanville and G. Henkelman, *J. Phys.: Condens. Matter*, 2009, **21**, 084204.
- 35 G. Mills and H. Jónsson, *Phys. Rev. Lett.*, 1994, **72**, 1124–1127.
- 36 M.-M. Rohmer, M. Benard, C. Henriet, C. Bo and J.-M. Poblet, *J. Chem. Soc., Chem. Commun.*, 1993, 1182–1185.
- 37 X. Zhang, Z. Ma, X. Zhao, Q. Tang and Z. Zhou, *J. Mater. Chem. A*, 2015, **3**, 4960–4966.
- 38 M. Naguib, O. Mashtalir, J. Carle, V. Presser, J. Lu, L. Hultman, Y. Gogotsi and M. W. Barsoum, *ACS Nano*, 2012, **6**, 1322–1331.
- 39 J. Li and R. Hoffmann, *Chem. Mater.*, 1989, **1**, 83–101.
- 40 R. Sumathi and M. Hendrickx, *Chem. Phys. Lett.*, 1998, **287**, 496–502.
- 41 C. Berkdemir, A. W. Castleman and J. O. Sofo, *Phys. Chem. Chem. Phys.*, 2012, **14**, 9642–9653.
- 42 S. Wang, J.-X. Li, Y.-L. Du and C. Cui, *Comput. Mater. Sci.*, 2014, **83**, 290–293.
- 43 M. A. Sobhy, A. W. Castleman and J. O. Sofo, *J. Chem. Phys.*, 2005, **123**, 154106.
- 44 J. I. Martinez, A. Castro, A. Rubio and J. A. Alonso, *J. Chem. Phys.*, 2006, **125**, 074311.
- 45 G. K. Gueorguiev and J. M. Pacheco, *Phys. Rev. Lett.*, 2002, **88**, 115504.
- 46 J. Tersoff and D. R. Hamann, *Phys. Rev. B: Condens. Matter*, 1985, **31**, 805–813.
- 47 S. Mogck, B. J. Kooi, J. T. M. De Hosson and M. W. Finnis, *Phys. Rev. B: Condens. Matter*, 2004, **70**, 245427.
- 48 J. C. Meyer, S. Kurasch, H. J. Park, V. Skakalova, D. Künzel, A. Groß, A. Chuvilin, G. Algara-Siller, S. Roth, T. Iwasaki, U. Starke, J. H. Smet and U. Kaiser, *Nat. Mater.*, 2011, **10**, 209–215.
- 49 L. Wu, Y. Zhu, T. Vogt, H. Su, J. W. Davenport and J. Taftø, *Phys. Rev. B: Condens. Matter*, 2004, **69**, 064501.
- 50 W. Li and N. Mingo, *Phys. Rev. B: Condens. Matter*, 2014, **90**, 094302.
- 51 S. Zhang, Q. Wang, X. Chen and P. Jena, *Proc. Natl. Acad. Sci. U. S. A.*, 2013, **110**, 18809–18813.
- 52 P. Liu, J. A. Rodriguez, H. Hou and J. T. Muckerman, *J. Chem. Phys.*, 2003, **118**, 7737–7740.
- 53 T. Tohei, A. Kuwabara, F. Oba and I. Tanaka, *Phys. Rev. B: Condens. Matter*, 2006, **73**, 064304.
- 54 K. Huang and M. Born, *Dynamical Theory of Crystal Lattices*, Clarendon, Oxford, 1954.
- 55 J. Wang, S. Yip, S. R. Phillpot and D. Wolf, *Phys. Rev. Lett.*, 1993, **71**, 4182–4185.
- 56 K. H. Michel and B. Verberck, *Phys. Rev. B: Condens. Matter*, 2009, **80**, 224301.
- 57 E. Cadelano, P. L. Palla, S. Giordano and L. Colombo, *Phys. Rev. B: Condens. Matter*, 2010, **82**, 235414.
- 58 G. N. Greaves, A. L. Greer, R. S. Lakes and T. Rouxel, *Nat. Mater.*, 2011, **10**, 823–837.
- 59 R. C. Andrew, R. E. Mapasha, A. M. Ukpogon and N. Chetty, *Phys. Rev. B: Condens. Matter*, 2012, **85**, 125428.
- 60 R. C. Cooper, C. Lee, C. A. Marianetti, X. Wei, J. Hone and J. W. Kysar, *Phys. Rev. B: Condens. Matter*, 2013, **87**, 035423.
- 61 J. Heyd, G. E. Scuseria and M. Ernzerhof, *J. Chem. Phys.*, 2003, **118**, 8207–8215.
- 62 J. Heyd, G. E. Scuseria and M. Ernzerhof, *J. Chem. Phys.*, 2006, **124**, 219906.
- 63 L. Z. Zhang, Z. F. Wang, S. X. Du, H. J. Gao and F. Liu, *Phys. Rev. B: Condens. Matter*, 2014, **90**, 161402.
- 64 Y. Xie, M. Naguib, V. N. Mochalin, M. W. Barsoum, Y. Gogotsi, X. Yu, K.-W. Nam, X.-Q. Yang, A. I. Kolesnikov and P. R. C. Kent, *J. Am. Chem. Soc.*, 2014, **136**, 6385–6394.
- 65 Y. Xie, Y. Dall'Agnese, M. Naguib, Y. Gogotsi, M. W. Barsoum, H. L. Zhuang and P. R. C. Kent, *ACS Nano*, 2014, **8**, 9606–9615.
- 66 Q. Tang, Z. Zhou and P. Shen, *J. Am. Chem. Soc.*, 2012, **134**, 16909–16916.
- 67 K. Persson, V. A. Sethuraman, L. J. Hardwick, Y. Hinuma, Y. S. Meng, A. van der Ven, V. Srinivasan, R. Kostecki and G. Ceder, *J. Phys. Chem. Lett.*, 2010, **1**, 1176–1180.
- 68 M. V. Koudriachova, N. M. Harrison and S. W. de Leeuw, *Solid State Ionics*, 2002, **152–153**, 189–194.
- 69 M. V. Koudriachova, N. M. Harrison and S. W. de Leeuw, *Solid State Ionics*, 2003, **157**, 35–38.
- 70 C. H. Sun, X. H. Yang, J. S. Chen, Z. Li, X. W. Lou, C. Li, S. C. Smith, G. Q. Lu and H. G. Yang, *Chem. Commun.*, 2010, **46**, 6129–6131.

Supplementary Information (SI)

**TiC<sub>2</sub>: A New Two Dimensional Sheet beyond MXenes**

Tianshan Zhao,<sup>a,b</sup> Shunhong Zhang,<sup>a,b</sup> Yaguang Guo,<sup>a,b</sup> and Qian Wang<sup>\*a,b</sup>

<sup>a</sup>Center for Applied Physics and Technology, College of Engineering, Peking University, Beijing 100871, China

<sup>b</sup>IFSA Collaborative Innovation Center, and Key Laboratory of High Energy Density Physics Simulation, Ministry of Education, Beijing 100871, China

E-mail: [qianwang2@pku.edu.cn](mailto:qianwang2@pku.edu.cn)

**1. Candidate structures of C<sub>2</sub> containing TiC<sub>2</sub>**

By depositing C<sub>2</sub> dimers on the surface of a monolayer triangular Ti lattice, we obtain three candidate structures of the 2D TiC<sub>2</sub> sheet.

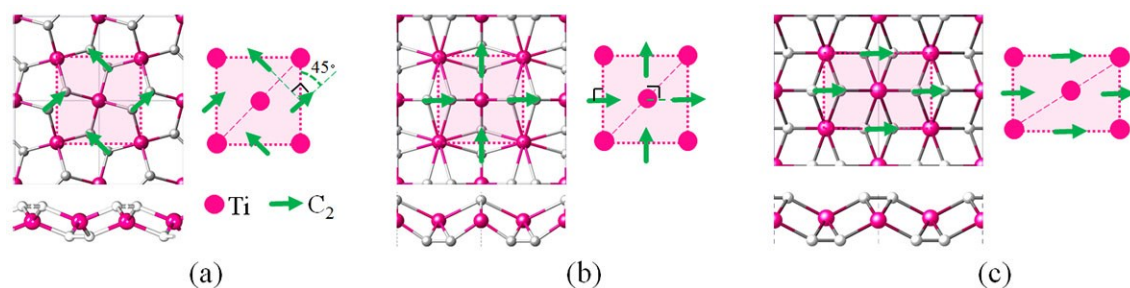


**Fig. S1** C<sub>2</sub> dimers inserted at different positions and with different orientations on the surface of a triangular Ti lattice. (a) C<sub>2</sub> dimers bind to Ti atoms in EOC mode, and perpendicular to the nearest neighboring C<sub>2</sub> dimers; (b) C<sub>2</sub> dimers bind to Ti atoms in both SOC and EOC modes, and perpendicular to the near neighboring C<sub>2</sub> dimers; (c) C<sub>2</sub> dimers bind to Ti atoms in both SOC and EOC modes, but are all parallelly aligned.



## 2. Stability relative to the 2D TiC<sub>2</sub> isomeric structures

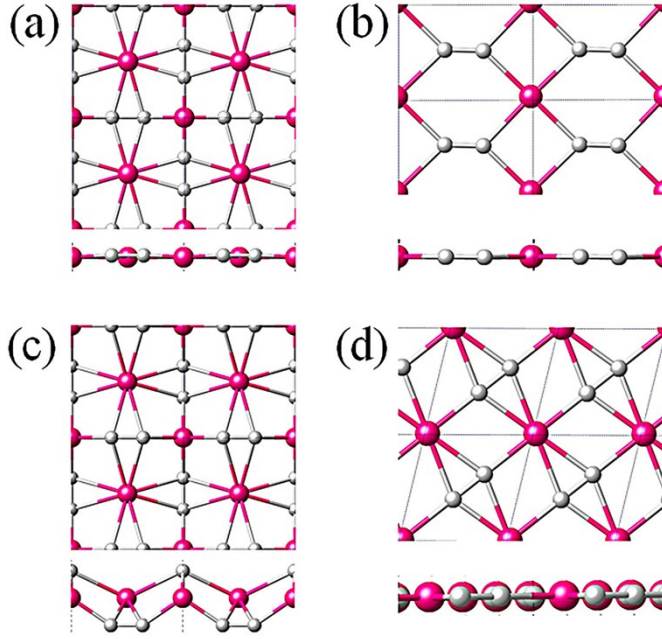


**Fig. S2** Two energetically low-lying structural isomers of TiC<sub>2</sub> containing C<sub>2</sub> units. (a) and (b) are the initial structures; (c) and (d) are the corresponding optimized structures, respectively.

## 3. Stability relative to other Ti-C compounds

For comparison, we calculated the cohesive energy of TiC<sub>2</sub>, Ti<sub>3</sub>C<sub>2</sub> (MXene), bulk TiC, and some other Ti-C binary compounds. To gauge the relative stability of a compound with the composition of Ti<sub>x</sub>C<sub>1-x</sub>, using the method described by Zhang et al.<sup>1</sup>, we define its molar formation energy  $\delta F$  as

$$\delta F(Ti_x C_{1-x}) = E_{coh}(Ti_x C_{1-x}) - x\mu_{Ti} - (1-x)\mu_C \quad (1)$$

where  $E_{coh}(x)$  is the cohesive energy of the system,  $\mu_{Ti}$  and  $\mu_C$  are the chemical potentials of the Ti and C atoms, respectively. The relative stability of different Ti<sub>x</sub>C<sub>1-x</sub> structures can be gauged by comparing their  $\delta F$ : higher  $\delta F$  means inferior stability. We here set  $\mu_C$  and  $\mu_{Ti}$  as the cohesive

energy of graphene and bulk *hcp* Ti. The results are summarized in Figure S3. A line connecting the cohesive energy of graphene and bulk Ti is used to estimate the stability of a Ti-C compound: a structure with cohesive energy below the line ( $\delta F \leq 0$ ) is stable against decomposing into graphene and Ti; when  $\delta F > 0$ , the structure becomes metastable or even unstable. The recently predicted single-layer t-TiC<sup>1</sup> has a positive  $\delta F$  and hence is metastable. In contrast, the TiC<sub>2</sub> structure in our work has a negative  $\delta F$ , -0.40 eV, indicating a thermodynamically stability. The experimentally identified bulk TiC and 2D MXene (Ti<sub>3</sub>C<sub>2</sub> and Ti<sub>2</sub>C) also have negative  $\delta F$ . One should note that some Ti-C clusters, even though with positive  $\delta F$ , have been experimentally synthesized.<sup>2,3</sup> Therefore, the single-layer TiC<sub>2</sub> is thermodynamically favorable and may be formed when suitable synthetic conditions are provided.

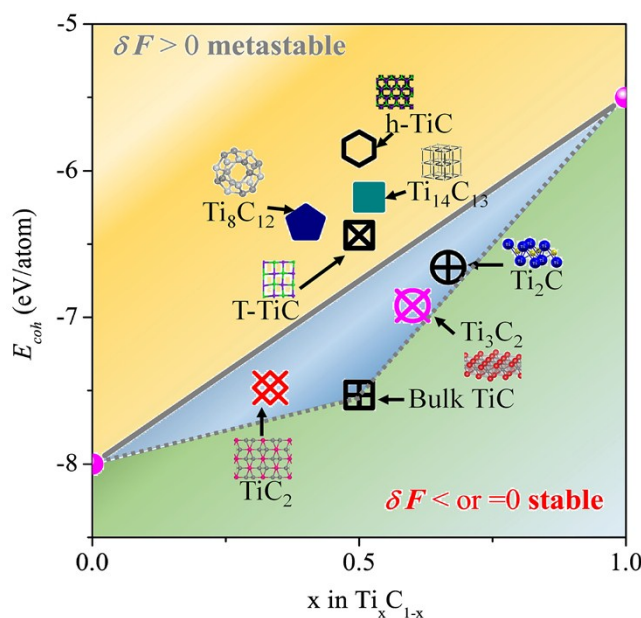


**Fig. S3** Cohesive energy for binary compounds with composition  $\text{Ti}_x\text{C}_{1-x}$ . The solid line links cohesive energies of graphene ( $x = 0$ ) and bulk Ti ( $x = 1$ ). Formation energy  $\delta F$  is positive (negative) above (below) the solid line.

#### 4. Stability relative to other isostructural metal carbides

We replace the Ti atoms in  $\text{TiC}_2$  sheet with other 3d transition metal atoms forming a series of 2D  $\text{MC}_2$  metal carbides. All structures are fully relaxed, and their cohesive energy are calculated as presented in Figure S4, which shows that  $\text{TiC}_2$  has the largest cohesive energy, indicating Ti atoms bind most strongly with  $\text{C}_2$  dimers in such structure.

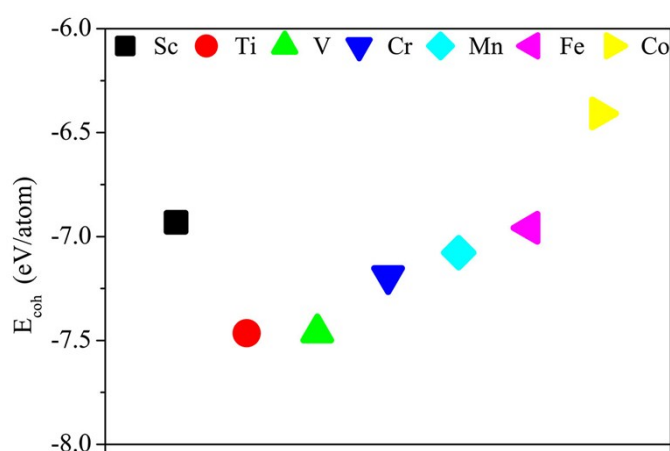


**Fig. S4** Cohesive energy of 2D transition metal dicarbides  $\text{MC}_2$  (M=Sc-Co) in the  $\text{TiC}_2$  structure.

#### 5. Thermal stability of the $\text{TiC}_2$ sheet



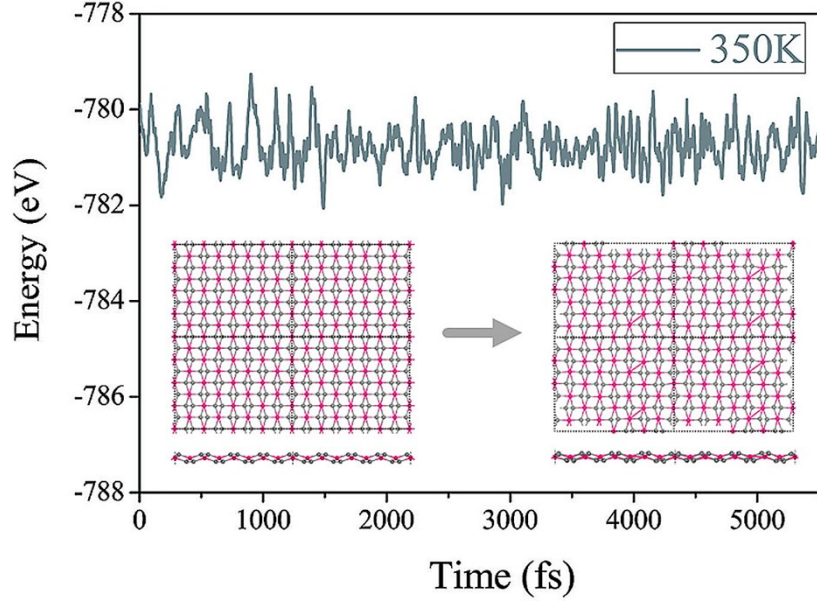


**Fig. S5** Evolution of potential energy of  $\text{TiC}_2$  during AIMD simulations at 350 K.  $4 \times 4 \times 1$  supercell is used to reduce the constraint of periodic condition in the axial direction. The insets show snapshots of atomic configurations at the beginning and the end of the simulations.

## 6. Electronic Properties of the $\text{TiC}_2$ sheet

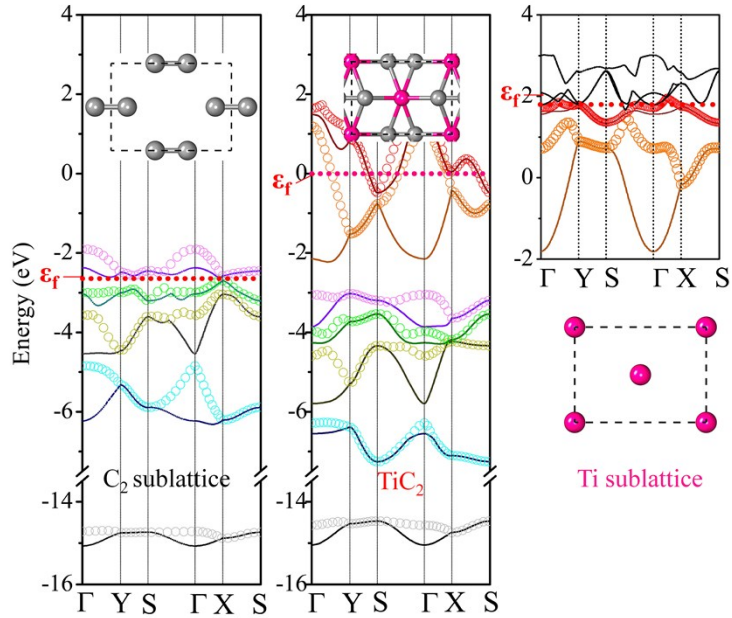


**Fig. S6** Band structure of the  $\text{TiC}_2$  sheet (center panel), the  $\text{C}_2$  sublattice (left panel), and Ti sublattice (right panel). The high symmetric k point path is along  $\Gamma (0, 0, 0) \rightarrow Y (0, 1/2, 0) \rightarrow$

$S (1/2, 1/2, 0) \rightarrow \Gamma (0, 0, 0) \rightarrow X (1/2, 0, 0) \rightarrow S (1/2, 1/2, 0)$ , corresponding to the axial direction in the real space.

## 7. Application of the $\text{TiC}_2$ sheet as Li ion battery anode material

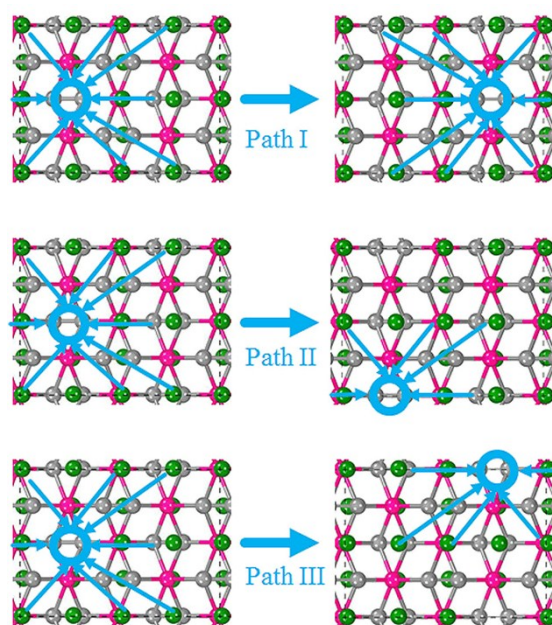


**Fig. S7** Considered migration paths of a Li “monovacancy” on the  $\text{TiC}_2$  sheet with the high coverage of  $\text{TiC}_2\text{Li}_2$ .

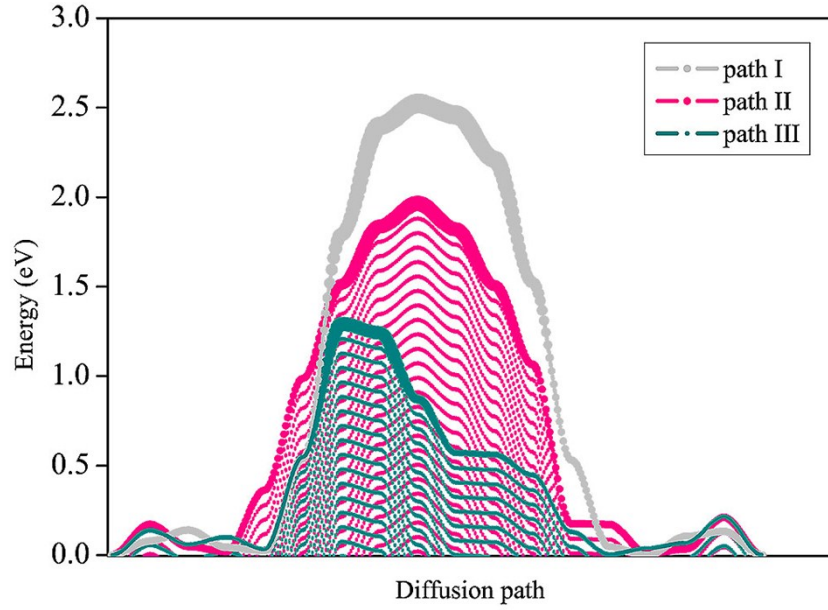
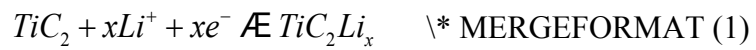


**Fig. S8** The energy barrier profiles of Li diffusion on  $\text{TiC}_2$  with the high coverage of  $\text{TiC}_2\text{Li}_2$ . The diffusion paths have been indicated in Figure S7.

#### Calculation Details: Estimation of the open circuit voltage (OCV)

Typically, the anode charge/discharge processes assume the following half-cell reaction that involves  $\text{Li}/\text{Li}^+$ :



The (OCV) for an intercalation reaction involving  $x \text{Li}^+$  ions is computed from the energy difference of the products and the reactants.

The electronic potential during this process can be written in the form of Gibbs free energy:

$$V = -\Delta G_f / zF \quad \backslash * \text{MERGEFORMAT (2)}$$

where  $z$  and  $F$  are the number of valence electrons during the adatom process and the Faraday constant, respectively;  $\Delta G_f$  is the change in Gibbs free energy during the adatom



process which is defined as:

$$\Delta G_f = \Delta E_f + P\Delta V_f - T\Delta S_f \quad \text{\textbackslash* MERGEFORMAT (3)}$$

$P\Delta V_f$  is on the order of  $10^{-5}$  eV and the term  $T\Delta S_f$  is comparable to 26 meV at low temperature.<sup>4,5</sup> Thus, the entropy (thermal) effects and pressure terms are negligible, and will not be discussed further.  $\Delta G_f$  is then approximately equal to the formation energy,  $\Delta E_f$ , involved in the adsorption process, which is defined as:

$$\Delta E_f = E(\text{TiC}_2\text{Li}_x) - E(\text{TiC}_2) - xE(\text{Li}) \quad \text{\textbackslash* MERGEFORMAT (4)}$$

Here  $E(\text{TiC}_2)$  denotes the total energy of pristine  $\text{TiC}_2$  monolayer,  $E(\text{Li})$  and  $E(\text{TiC}_2\text{Li}_x)$  are the total energy of bulk bcc Li and the lithiated  $\text{TiC}_2$  sheet ( $x$  Li atoms adsorbed in one supercell), respectively. The OCV is related to the formation energy by:

$$OCV = \Delta G_f / x \approx \Delta E_f / x = [E(\text{TiC}_2) + xE(\text{Li}) - E(\text{TiC}_2\text{Li}_x)] / x \quad \text{\textbackslash*}$$

MERGEFORMAT (5)

## References

1. Z. Zhang, X. Liu, B. I. Yakobson and W. Guo, *J. Am. Chem. Soc.*, 2012, **134**, 19326- 19329.
2. B. C. Guo, K. P. Kerns and A. W. Castleman, *Science*, 1992, **255**, 1411-1413.
3. J.S.Pilgrim and M.A.Duncan, *J. Am. Chem. Soc.*, 1993, **115**, 9724-9727.
4. M. K. Aydinol, A. F. Kohan, G. Ceder, K. Cho and J. Joannopoulos, *Phys. Rev. B*, 1997, **56**, 1354-1365.
5. A. Van der Ven, M. K. Aydinol, G. Ceder, G. Kresse and J. Hafner, *Phys. Rev. B*, 1998, **58**, 2975-2987.